

Atmospheric characterization of HIP 67522 b with VLT/CRIRES+ VLT/CRIRES+ suggests a heavier planet and hints at deuterium fractionation

A. Lavail¹, F. Debras¹, B. Klein², E. Chabrol³, S. Vinatier³, T. Hood⁴, A. Masson⁵, J. V. Seidel⁴, C. Moutou¹, S. Aigrain², A. Meech⁶, and O. Barragán^{2,7}

¹ Institut de Recherche en Astrophysique et Planétologie, Université de Toulouse, CNRS UMR 5277, 14 avenue Edouard Belin, 31400 Toulouse, France
e-mail: astro@lavail.net

² Department of Physics, University of Oxford, Oxford OX1 3RH, UK

³ LIRA, Observatoire de Paris, Université PSL, CNRS, Sorbonne Université, Université Paris Cité, 5 place Jules Janssen, 92195 Meudon, France

⁴ Laboratoire Lagrange, Observatoire de la Côte d'Azur, CNRS, Université Côte d'Azur, Nice, France

⁵ Centro de Astrobiología (CAB), CSIC-INTA, Camino Bajo del Castillo s/n, 28692, Villanueva de la Cañada, Madrid, Spain

⁶ Center for Astrophysics | Harvard & Smithsonian, 60 Garden St, Cambridge, MA 02138, USA

⁷ Department of Physics, University of Warwick, Coventry CV4 7AL, UK

Received January 30, 2026

ABSTRACT

Context. Young transiting exoplanets provide unique opportunities to probe planetary atmospheres during the critical early phases of evolution when atmospheric escape and contraction are most active. HIP 67522 b, a 17 Myr old hot Jupiter with an extraordinarily low bulk density ($< 0.10 \text{ g cm}^{-3}$), represents an ideal target for high-resolution transmission spectroscopy.

Aims. We aim to characterize the atmospheric composition, thermal structure, and dynamics of HIP 67522 b using ground-based high-resolution near-infrared spectroscopy with VLT/CRIRES+, complementing recent JWST observations.

Methods. We obtained 92 high-resolution spectra ($R \approx 10^5$) with VLT/CRIRES+ in the K2166 band during a transit on 30 January 2025. We applied cross-correlation techniques and Bayesian nested sampling retrievals to constrain molecular abundances, temperature structure, and atmospheric dynamics.

Results. We detect H₂O at 20σ and CO at 5σ , confirming the extremely extended atmosphere of this low-mass giant. A velocity offset of $-2.9 \pm 0.2 \text{ km s}^{-1}$ indicates day-to-night winds. The rotation velocity is constrained to $< 1.8 \text{ km s}^{-1}$ at 3σ , consistent with tidal locking. Retrieval analysis suggests a planetary mass of 29.8 ± 3 Earth masses and a vertically isothermal atmosphere. This mass is two times larger than the mass estimated from JWST atmospheric observations and inconsistent at 3σ hence leaving a doubt on the actual planetary density of the planet. Using the mass derived from the CRIRES+ data, we derive a C/O ratio of 0.83 ± 0.09 , about 1.5 times solar, and a subsolar metallicity $[\text{C+O/H}] = -0.8 \pm 0.4$ which can be increased if the atmosphere is cloudy, a degeneracy our data alone cannot resolve. We report a tentative 2σ detection of HDO with an extreme enrichment factor of ~ 1000 relative to the protosolar D/H ratio. If confirmed, this would be the first detection of deuterium in an exoplanet atmosphere and would require intense escape rate to be explained.

Key words. Techniques: spectroscopic – Planets and satellites: atmospheres – Planets and satellites: individual: HIP 67522

1. Introduction

Young transiting exoplanets ($< 100 \text{ Myr}$) represent crucial laboratories for understanding planetary formation as they allow direct observation of planets still undergoing contraction, cooling, and atmospheric escape. These systems provide empirical benchmarks for theories of evolution during the critical first hundred million years. Probing the atmospheres of these young planets provides a unique window into the early stages of planetary evolution, when key processes such as atmospheric escape and orbital migration are most active (Owen 2019; Baruteau et al. 2016). The atmospheric composition, temperature structure, and dynamics of young planets carry the imprint of their formation history. However, characterizing young planetary atmospheres remains challenging. Only a handful of stars younger than 100 Myr are known to host transiting planets, and their youth manifests as high magnetic activity—frequent flares

and starspots—that complicates the determination of planetary masses and atmospheric properties (e.g. Rackham et al. 2018). The youngest confirmed transiting systems include TIDYE-1b ($\sim 3 \text{ Myr}$; Barber et al. 2024), a Jupiter-sized planet still embedded in its natal disk, TOI-1227 b ($\sim 8 \text{ Myr}$; Mann et al. 2022), K2-33 b ($\sim 5\text{--}10 \text{ Myr}$; Mann et al. 2016), AU Mic b and c ($\sim 20\text{--}24 \text{ Myr}$; Plavchan et al. 2020), the remarkable four-planet V1298 Tau system ($\sim 23 \text{ Myr}$; David et al. 2019) and the puzzling planet HIP 67522 b ($\sim 17 \text{ Myr}$; Rizzuto et al. 2020).

HIP 67522 (=HD 120411) is a 17 Myr old early G star in the Sco-Cen association at a distance of 127 pc (Rizzuto et al. 2020). It hosts what was thought to be the youngest known transiting hot Jupiter because of its radius of $\sim 10 \text{ R}_\oplus$, HIP 67522 b, with an orbital period of 6.96 days (Rizzuto et al. 2020), and a second outer planet at 14.33 days (Barber et al. 2024). Heitzmann et al. (2021) constrained the projected obliquity of the planet to be $|\lambda| = 5.8_{-5.7}^{+2.80} \text{ }^\circ$. Recent JWST/NIRSpec observations have re-

vealed that HIP 67522 b has an extraordinarily low bulk density ($< 0.10 \text{ g cm}^{-3}$) and suggested a mass of only $13.8 \pm 1.0 \text{ M}_\oplus$ (Thao et al. 2024). This extremely low density translates into an atmospheric scale height comparable to the planetary radius itself, making HIP 67522 b one of the most favorable targets for atmospheric characterization. The JWST transmission spectrum showed strong detections of H_2O and CO_2 ($\geq 7\sigma$), with modest detection of CO (3.5σ), indicating a metal-enriched atmosphere with $3\text{--}10\times$ solar metallicity and a near-solar to sub-solar C/O ratio (Thao et al. 2024).

Recent photometric monitoring campaigns with TESS and CHEOPS have revealed a remarkable property of this system: the orbital period of HIP 67522 b exhibits significant clustering of stellar flares, with an approximately nine-times higher flare rate occurring in the 20% of the orbit immediately following planetary transit (Ilin et al. 2025b). This represents a robust detection of planet-induced stellar flaring. Follow-up radio observations at 1.1–3.1 GHz with ATCA confirmed strong radio activity consistent with coronal emission of cool dwarfs but did not detect the expected electron cyclotron maser emission (ECME) signature of magnetic star-planet interaction, placing upper limits of $< 0.7\%$ on the conversion efficiency of interaction power into radio waves (Ilin et al. 2025a).

Ground-based high-resolution spectroscopy (HRS) in the near-infrared provides a complementary approach to space-based observations, with the ability to simultaneously constrain atmospheric composition, temperature structure, and dynamics through the Doppler shifts and line broadening of molecular absorption features (Snellen et al. 2010; Brogi et al. 2016). In this paper, we present VLT/CRIRES+ high-resolution transmission spectroscopy of HIP 67522 b in the K band (centred at 2166 nm), obtained during a transit on 30 January 2025. Our observations and data reduction are presented in Sect. 2, the cross-correlation analysis and atmospheric retrievals are detailed in Sect. 3 and we discuss our results in Sect. 4.

2. Observations and data reduction

2.1. Description of the observations

We observed HIP 67522 during a transit of the exoplanet HIP 67522 b. We used the high-resolution near-infrared spectrograph CRIRES+ (Dorn et al. 2023) mounted at the 8-metre Unit Telescope 3 of the Very Large Telescope on the 30th January 2025 (ESO Programme 114.28HP.001, PI: Klein). Our observations started at 04:28 UT, ended at 09:18 UT and consisted of 92 consecutive spectra each taken with a detector integration time of 180 seconds. The observations were carried out in nodding mode, meaning that the target was alternatively positioned on two distinct positions (A and B) on the slit. The nodding procedure facilitates the data reduction and the removal of sky and instrumental background.

We used CRIRES+ in the K2166 wavelength setting covering the wavelength range between 1990 and 2472 nm over 6 spectral orders – note that there are wavelength gaps between the orders. Metrology was activated during the acquisition to improve the accuracy of the wavelength solution. The $0.2''$ slit was set up yielding the nominal resolving power of $R \approx 10^5$. This dataset does not suffer from the known super-resolution issue (e.g. Nortmann et al. 2025) affecting CRIRES+ spectra for which the point spread function (PSF) is smaller than the slit width. In this case, we did not use the adaptive optics system, and the PSF stayed larger than the slit throughout the observations. The seeing increased drastically in the last third of the transit and

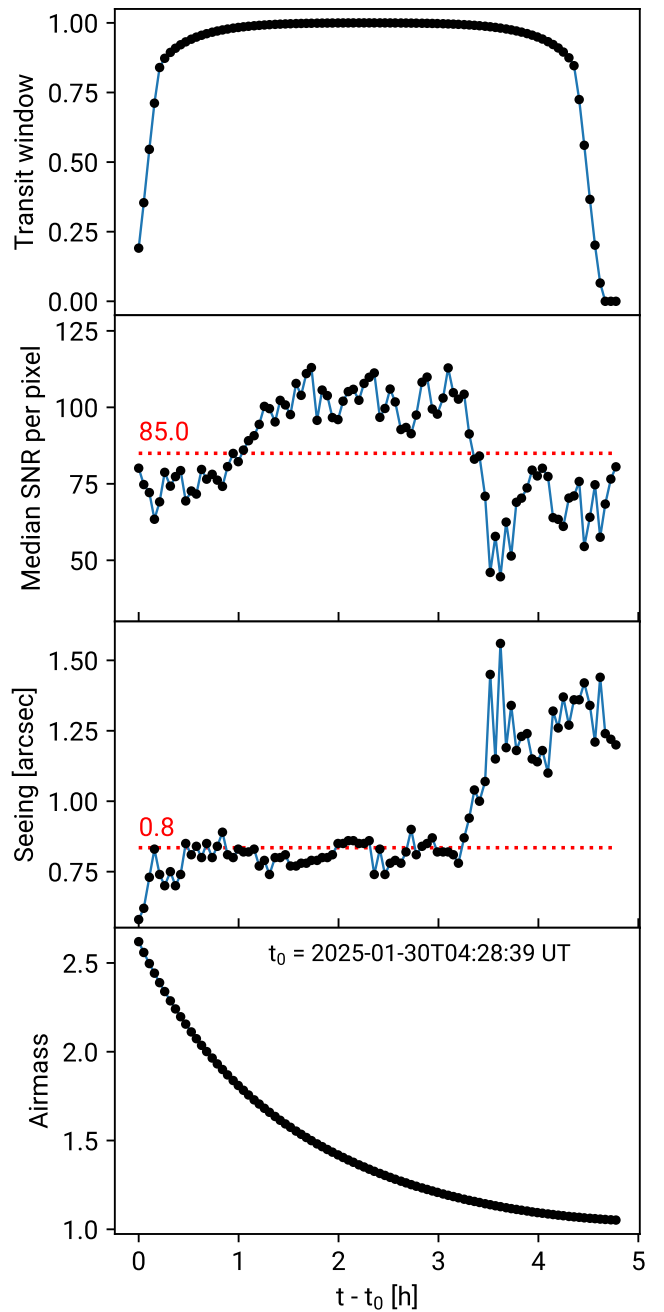


Fig. 1. Evolution of the transit window, the median SNR per exposure, seeing, and airmass as a function of time from the first exposure. The median SNR and median seeing for the full time-series are indicated in red on the second and third panel respectively. The UT time at the start of the first exposure t_0 is indicated on the fourth panel.

decreased the signal-to-noise ratio (SNR) accordingly despite an improving airmass (Fig. 1).

2.2. Data reduction

The data were reduced with the CRIRES+ data reduction system (DRS) `cr2res` available from the ESO website¹. In a first step, the raw calibrations (flat fields, darks, Fabry-Perot etalon, Uranium-Neon lamp) taken as part of the VLT daily calibration

¹ <https://www.eso.org/sci/software/pipelines/cr2res/>

routine and associated to our science data were reduced using the standard calibration cascade, as described in the CRIRES+ pipeline user manual. This step yields reduced calibrations : (1) normalized flat fields characterising pixel-to-pixel sensitivity variations, (2) a bad pixel mask, and (3) a so-called tracewave file containing the locations of the spectral orders on the detectors, the slit curvature, and the wavelength solution. In a second step, reduced calibrations are applied to pairs of spectra taken in nodding positions A and B. Finally, 1D spectra are extracted with the `cr2res_obs_nodding` recipe. This step provides the time-series of 92 1D wavelength-calibrated spectra.

After the DRS reduction, we apply `molecfit` on the mean A and B spectra to further improve the wavelength solutions for the A and B nodding position. We then interpolate the B spectrum into the wavelength solution of the A spectrum. We also compute the BJD TDB (Barycentric Julian Date in the Temps Dynamique Barycentrique time scale) timestamp at midexposure for each spectra as well as the barycentric velocity correction (BERV) using `barycorrpy` (Kanodia & Wright 2018).

2.3. Additional post-processing steps

After this initial data reduction, the data are shaped so that we apply the ATMOSPERIX pipeline² to reduce transmission spectroscopy data and extract planetary signal (Klein et al. 2024; Debras et al. 2024). The pipeline is made up of different steps, summarised as follows.

1. The spectra are all aligned in the stellar rest frame, from which a master-out spectrum I_{ref} is created usually by averaging out-of-transit exposures. In our case, because we have too few baseline observations, the master spectrum encompasses all exposures. This master spectrum is then moved back to the geocentric frame and linearly matched in flux to each of the observed spectra, which are each divided by its best-fitting solution. The resulting spectra are then divided by a second master spectrum, now in the Earth rest frame, to provide an additional correction of the tellurics.
2. A normalisation of each of the resulting spectra is then performed using an estimate of the noise-free continuum, calculated using a rolling mean window of 150 pixel. This is followed by a 5σ clipping being applied to remove outliers. This two-step process is then repeated until there are no more outliers flagged in the data.
3. As some pixels with high temporal variance might remain, we calculated the variance for each pixel and applied an iterative parabolic fit to the pixel variance distribution. We considered pixels further than 5σ from the fit as outliers and masked them out for the rest of the data-reduction process.
4. Finally, we further correct remaining correlated noise through the use of a principal component analysis (PCA). In this study, we removed 6 principal components for each CRIRES+ order, as fewer components did not allow to correct the tellurics properly and we could observe their influence in the $K_p - \nu_{\text{sys}}$ map up to 5 principal components.

Applying a PCA to the data also affects the planetary signal, degrading it. To take into account this degradation, we implemented the method of Gibson et al. (2022). For this, during the data-reduction process, we keep a matrix \mathbf{U} of the removed eigenvectors for each order which by construction is associated with correlated noise. These are subsequently used to prepare the synthetic spectra for analysing the data to degrade

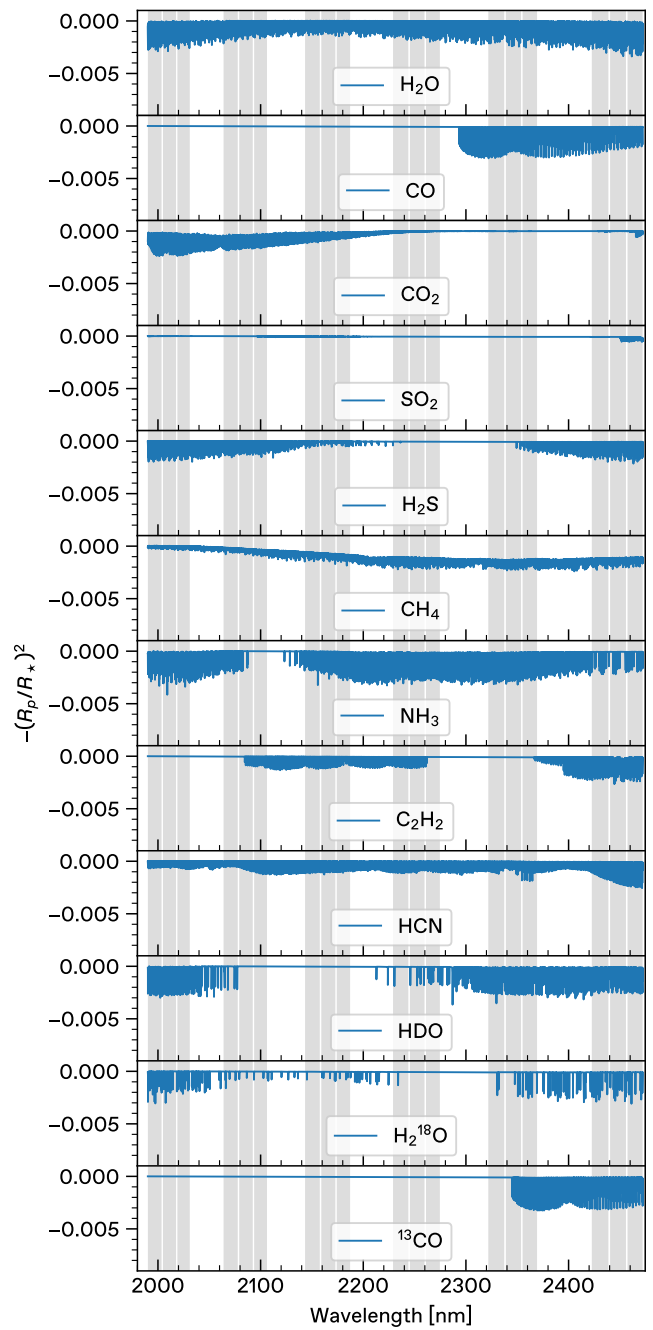


Fig. 2. Model isothermal spectra for each of the chemical species we investigated in the atmosphere of HIP 67522 b. The gray shaded areas represent the wavelength coverage of CRIRES+ with six spectral orders each spread over three detectors.

them coherently with the real signal. We have shown that using this method in our ATOMSPHERIX pipeline allows to retrieve unbiased physical parameters of the planetary atmosphere using synthetic data in Klein et al. (2024), excluding statistical sources of biases discussed in Debras et al. (2024).

3. Cross-correlation maps and Bayesian exploration

3.1. Detection of H_2O and CO through correlation

Once the data is reduced, we searched for molecular absorption in the atmosphere of HIP 67522 b starting by species detected by

² https://github.com/baptklein/ATOMSPHERIX_DATA_RED

JWST (H_2O , CO , CO_2 and H_2S) and extending to other plausible species in the atmosphere, based on thermo-chemical models (CH_4 , NH_3 , C_2H_2 , and HCN). The physical values used for our models are gathered in Table 1. Note that the mass is almost two times the mass derived from JWST observations in Thao et al. (2024). This is explained and justified in Sect. 3.2.1.

We created isothermal models of the planet atmosphere (Fig. 2) using *petitRADTRANS* (Mollière et al. 2019; Blain et al. 2024) containing only one of each of these species with a mass mixing ratio of 10^{-3} and correlated these models with our reduced data. This gives the so-called K_p - v_{sys} map where a detection is validated when the maximum of correlation is significantly larger than the noise level, at the expected orbital semi-amplitude of the planet and at physically sound Doppler shifts. The isothermal model spectra for each species are shown in Fig. 2.

Through this method, we detected H_2O at 20σ and CO at 5σ (Fig. 3). Here, σ is evaluated from the standard deviation of the noise in the K_p - v_{sys} map (selecting the area of the map where planetary signals and telluric residuals are absent). Under this definition, a 20σ detection corresponds to a correlation signal 20 times stronger than the noise standard deviation. We did not detect any of the other available species through this method, some of them like SO_2 being almost impossible to detect in the K-band due to their lack of strong absorption lines. The extremely high level of detection of water and carbon monoxide compared to usual detections in near infrared high resolution spectroscopy confirms an extremely extended atmosphere, hence a low-mass planet.

The maximum of detection occurs at a velocity of -3 km.s^{-1} relatively to the systemic velocity, which indicates day-to-night winds on the limbs of the planet. We adopted a systemic velocity of $v_{\text{sys}} = 7.41 \pm 0.25 \text{ km s}^{-1}$ (Rizzuto et al. 2020). The exact value of these winds is difficult to measure, as the star is a fast rotator. Nonetheless, regarding the results by different instruments at different epoch in Rizzuto et al. (2020, Table 2), the systemic velocity of the star appears rather superior to the value we chose, and hence the wind speed is more likely underestimated.

3.2. Bayesian exploration through nested sampling

3.2.1. Simple isothermal models

In order to constrain further the atmospheric composition and thermodynamics, we then ran nested sampling retrievals, based on the *PyMultiNest* code (Feroz & Hobson 2008; Feroz et al. 2009; Buchner et al. 2014). We first used isothermal models for simple constraints on the planet and its atmosphere and we started by looking for an independent estimation from JWST on the mass of the planet. Note that the mass is not directly a parameter of the retrieval, as the physical quantity that impacts the atmosphere scale height is gravity. We therefore define here "mass" as:

$$M = \frac{gR_{\text{TESS}}^2}{G} \quad (1)$$

where g is the gravity that we retrieve, G is the gravitational constant and $R_{\text{TESS}} = 0.892 R_J$ the best fit radius from TESS observations with R_J the Jupiter mean radius and assuming a stellar radius of $1.38 R_{\odot}$ with R_{\odot} the solar radius.

Because the radius of the planet is extremely dependent on the wavelength, as the atmosphere is almost the size of the planet, we included the TESS radius in our retrievals by defining

a TESS likelihood (where the constant terms are neglected as in Brogi & Line 2019):

$$\ln \mathcal{L}_{\text{TESS}} = -\frac{1}{2} \frac{((R_p/R_{\star})_{\text{TESS}} - (R_{p,\text{retrieved}}/R_{\star}))^2}{\sigma_{\text{TESS}}^2} \quad (2)$$

where R_p is the planetary radius, R_{\star} the stellar radius, TESS subscript indicates the TESS observations, "retrieved" indicates the retrieved value by our nested sampling algorithm. To calculate the TESS radius in our observations, we integrated the radius obtained in our isothermal models multiplied by the instrumental response of TESS in its wavelength range of observation.

Contrary to low resolution observations, we are not able to directly compare our best-fit model to the data, as they are drowned under the noise. We therefore follow Brogi & Line (2019) and include a scaling parameter a in the high resolution spectroscopy likelihood:

$$\ln \mathcal{L}_{\text{HRS}} = -\frac{1}{2} \sum_n \frac{(\text{data}[n] - a * \text{model}[n])^2}{\sigma[n]^2} \quad (3)$$

where $\text{data}[n]$ is the data at each pixel, $\text{model}[n]$ the value of the retrieved model during the bayesian exploration at the same pixel and $\sigma[n]$ the observational uncertainty at each pixel, defined by the standard deviation in time of each pixel as in Klein et al. (2024). Our models can be considered correct when the retrieved a distribution is centered around 1. As in Brogi & Line (2019), our total likelihood is simply:

$$\ln \mathcal{L}_{\text{tot}} = \ln \mathcal{L}_{\text{TESS}} + \ln \mathcal{L}_{\text{HRS}} \quad (4)$$

Note that we do not include $a\beta$ parameters to scale the noise as we follow the method of Gibson et al. (2020) that derives the likelihood with respect to this parameter to minimize its value.

The parameters of our isothermal retrieval are therefore K_p , V_{sys} , isothermal temperature, water and carbon monoxide mass mixing ratios (MMR), a corrective factor for gravity (dg), a corrective factor for radius (dR) and the a factor in the likelihood. Firstly, including the end of the transit, where the seeing gets two times larger than during the beginning of the night (see Fig. 1), biases our retrievals towards unrealistic values of K_p excluding the expected planetary value at 2σ . However, when considering only the low-seeing part of the observation, we do retrieve that the posterior for orbital velocity is centered on the expected planetary value. In the rest of the bayesian exploration, we therefore limit ourselves to the exposures before the drastic increase of the seeing.

Regarding mass constraints, we obtain that dg is directly correlated with the a value, which is expected as the size of the atmosphere is directly proportional to gravity (see notably the discussion in Debras et al. 2024). We therefore only kept dg and fixed $a = 1$ in the likelihood. This gives us a retrieved mass of 29.8 ± 2.9 Earth masses for the planet (1σ errorbar) which is about two times the mass retrieved by Thao et al. (2024). We are therefore inconsistent with their mean retrieved mass at 5σ . We discuss this discrepancy in Sect. 4.1.

With these isothermal models we confirmed the detection of H_2O and CO and were able to put constraints on the maximum MMR of other species as detailed in Table 2. We also confirmed a wind speed of $-2.9 \pm 0.2 \text{ km.s}^{-1}$, consistent with our correlation maps.

With our isothermal retrieval, only considering water and CO we obtain a C/O ratio of 0.83 ± 0.09 , which is about 1.5 times solar. Note that we are limited to C/O ratio inferior or equal to 1 as

Table 1. Adopted HIP 67522 system parameters

Stellar parameters	Value	Reference
Mass (M_{\odot})	1.22	Rizzuto et al. (2020)
Radius (R_{\odot})	1.38	Rizzuto et al. (2020)
Effective temperature (K)	5675	Rizzuto et al. (2020)
Systemic velocity (km.s ⁻¹)	7.4	Rizzuto et al. (2020)
Planetary parameters	Value	Reference
Epoch of transit (T_0)	2458604.02376	Barber et al. (2024)
Orbital Period (days)	6.9594731	Barber et al. (2024)
Mass (M_J)	0.088	This work
Mass (M_{Earth})	29.8	This work
1 σ Mass uncertainty (M_{Earth})	2.9	This work
Planet-star radius ratio	0.0668	Rizzuto et al. (2020)
Uncertainty on planet-star radius ratio σ_{TESS}	0.001	Rizzuto et al. (2020)
Radius (R_J)	0.892	Rizzuto et al. (2020)
g (m.s ⁻²)	2.8	This work
Planet RV semi-amplitude (km.s ⁻¹)	120	Barber et al. (2024)
Semi-major axis (au)	0.075	Barber et al. (2024)
Inclination (deg)	89.3	Rizzuto et al. (2020)
Eccentricity	0.0	Fixed
Transit duration (h)	4.82	Rizzuto et al. (2020)
Equilibrium Temperature (K)	1100	Rizzuto et al. (2020)

Table 2. Molecular abundances from isothermal retrievals. We considered that the 1 σ abundances were more constrained than upper limits when (i) the posterior showed a peak, and not a flat uniform distribution and (ii) the lower 1 σ abundance limit was superior to -9. The HDO distribution has the highest peak of all molecules (excepting H₂O and CO), and the only one with a 2 σ lower bound > -9.

Molecules	1 σ Abundance ($\log_{10}(\text{MMR})$)	3 σ Abundance ($\log_{10}(\text{MMR})$)
H ₂ O	$\in [-3.6, -3.1]$	$\in [-4.1, -2.4]$
CO	$\in [-2.8, -2.0]$	$\in [-3.5, -1.1]$
CO ₂	< -5.2	< -3.3
SO ₂	$\in [-8.5, -2.8]$	< -1.
H ₂ S	< -4.7	< -2.9
CH ₄	< -6.4	< -4.8
NH ₃	$\in [-7.2, -5.2]$	< -4.4
HCN	$\in [-7.4, -3.6]$	< -2.7
C ₂ H ₂	< -5.6	< -3.9
HDO	$\in [-5.6, -4.4]$	< -3.4
H ¹⁸ O	< -5.6	< -3.5
¹³ CO	< -4.6	< -2.8

we only retrieve water and CO, and that might bias our retrieved ratio towards lower values (see discussion in Hood et al. 2024). We further derive a metallicity [C+O/H] of -0.8 ± 0.4 , excluding a solar-like metallicity at 2 σ . Both these results are inconsistent with Thao et al. (2024), and we discuss it further in Section 4.

We included the possibility for an opaque cloud deck, and we obtain the usual result that clouds are degenerated with metallic-

ity (without affecting the C/O ratio): a higher metallicity leads to an absorption that can occur above the cloud deck, provided the clouds are deeper than 0.1 mbar. As discussed in Sect. 4, we are not able to resolve this degeneracy, and would need additional observations at different wavelength ranges.

We also put constraints on the rotation speed of the planet using the efficient rotational kernel detailed in the appendix of

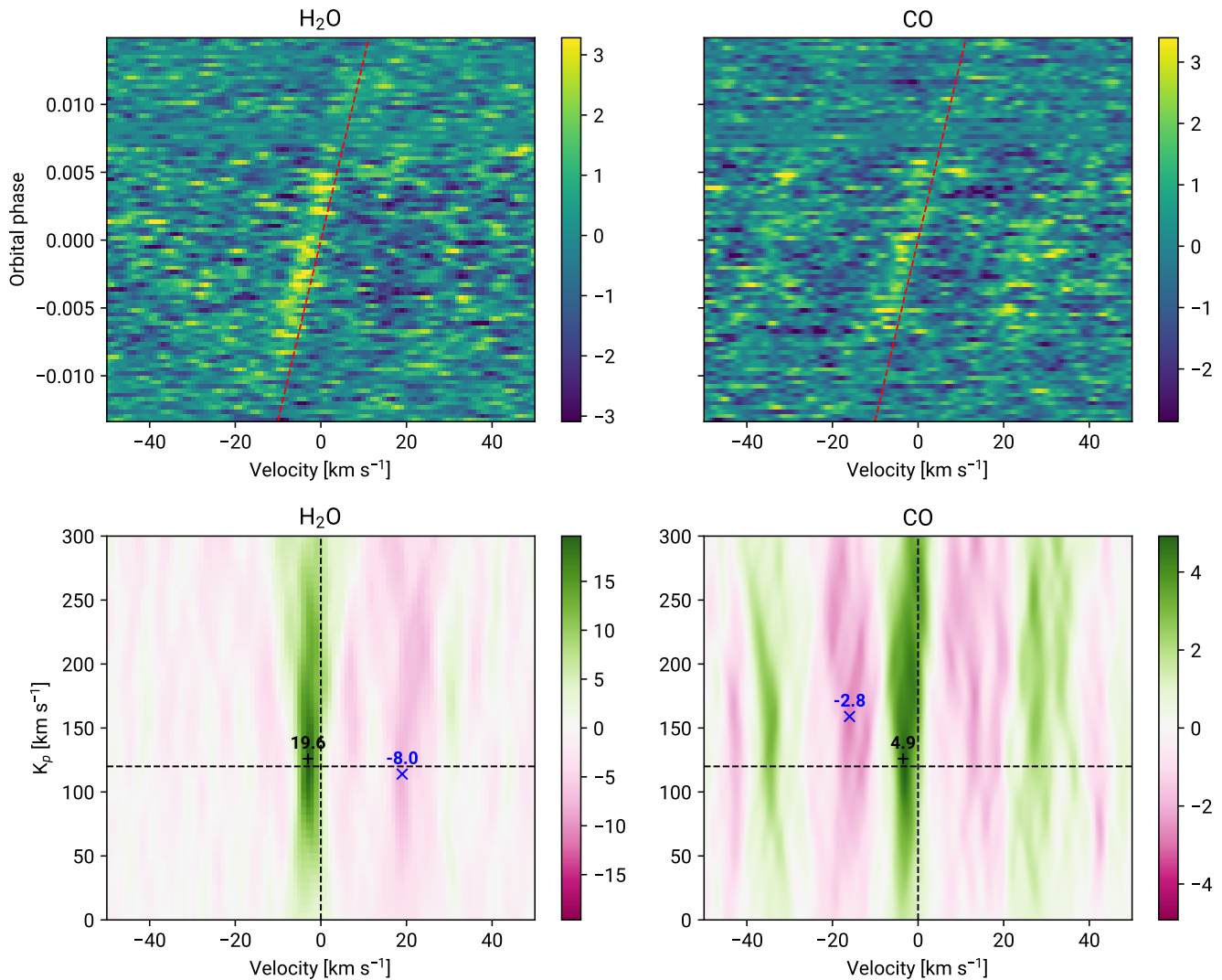


Fig. 3. Top panel: Phase- v_{sys} maps for the detected species H_2O (left) and CO (right) in the stellar reference frame. The red dashed line indicate the predicted velocity trail of the planet. The colorbar are expressed in standard deviations away from both planet and tellurics signals (excluding the square in the K_p - v_{sys} map defined by $K_p \in [0, 300]$ and $V_{\text{sys}} \in [-10, 30]$). Bottom panel: K_p - v_{sys} map for H_2O (left) and CO (right), the vertical dashed line indicate stellar reference frame, the horizontal dashed line indicated $K_p = 120 \text{ km s}^{-1}$. The maximum value of the map is indicated by the + symbol in black with the associated value, the minimum is indicated by the blue cross.

Klein et al. (2024). We only obtained an upper limit: the data favour a rotation speed at the equator inferior to 0.9 km.s^{-1} at 1σ and 1.8 km.s^{-1} at 3σ . This is consistent with tidal locking and excludes Jupiter-like rotation speed (around 10 km.s^{-1} at the equator). Given the fact that the atmosphere is about the size of the planet, tidal locking would yield a rotation speed of 0.4 km.s^{-1} at the equator around 1 bar and up to 0.8 km.s^{-1} at 0.1 mbar pressure.

In the rest of the paper, we decided to fix the mass to our most likely retrieved value with isothermal models, 29.8 Earth masses. This is a strong limitation but including the mass in models of higher complexity leads to very large degeneracies which prevent to draw any conclusion on the atmospheric structure. Additionally, as discussed in Sect. 4.2, the evidence ratio favors models with a fixed mass with a Bayes factor superior to 5. In other words, including the mass uncertainty in the retrieval leads to better fit of the data but with a larger parameter space, which leads to a statistical preference towards model us-

ing a fixed mass. With these caveats in mind, we therefore restrict further analysis to a mass fixed at our retrieved value.

In Fig. 4, we show the posterior densities of the parameters of our isothermal model including HDO (see Sect. 3.2.3), that shows visually the results with our best retrieved mass as discussed here and in the rest of the paper.

3.2.2. More complex profiles: vertical or horizontal structure

Because of the extremely high signal to noise ratio obtained in cross correlation maps, we decided to go a step further in the usual bayesian analysis and included more complex modelling of the atmosphere. Our first test was to include the possibility for two temperatures: a temperature in the high atmosphere and a temperature in the deep atmosphere, with the pressure at which the temperature changes included as a free parameter in the retrieval. The retrieval converged towards two models: one where the change of pressure is at depth (deeper than 1mbar), the deep temperature is unconstrained and the shallow temperature is sim-

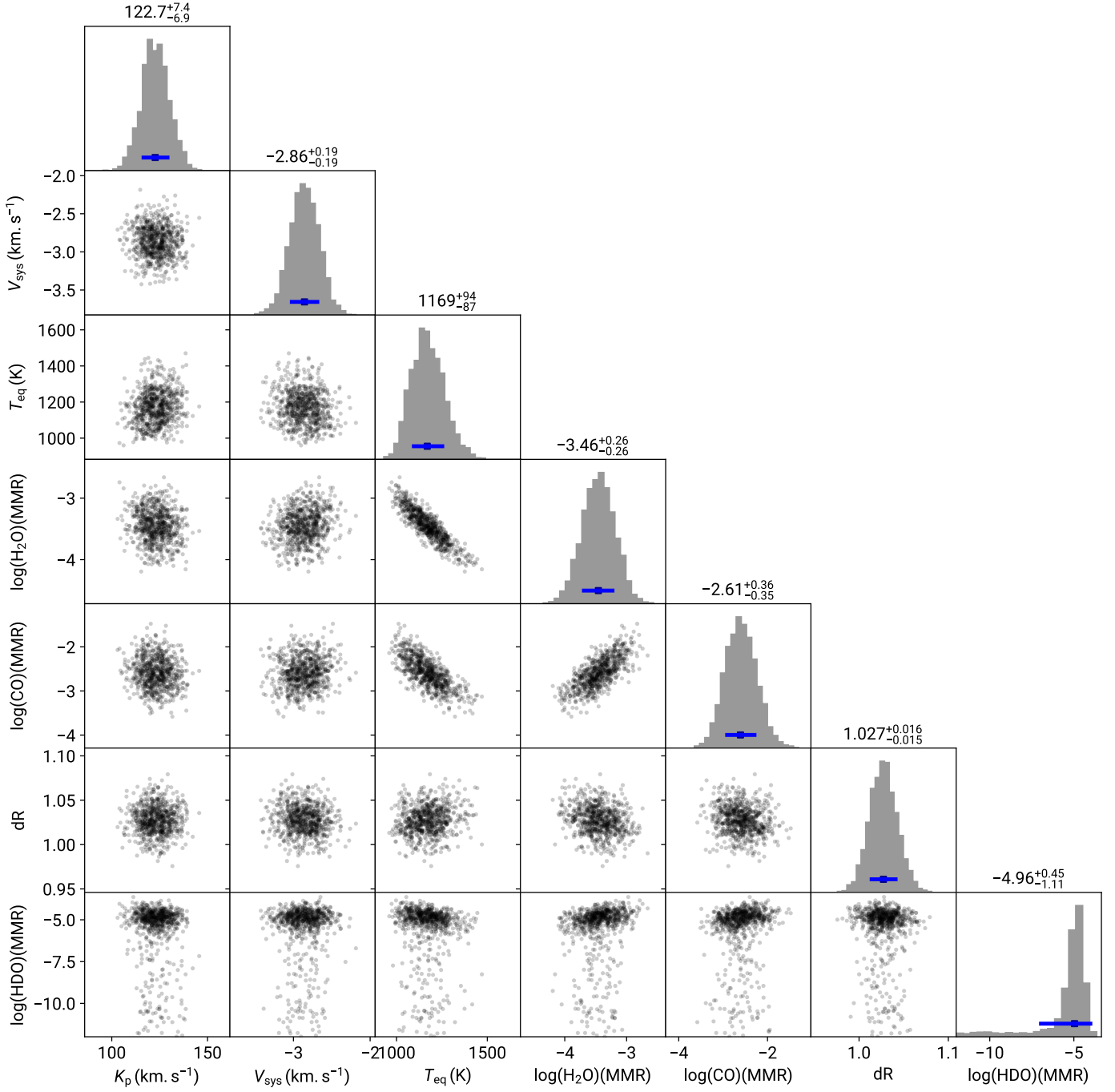


Fig. 4. Corner plot of the posterior distribution of our isothermal models using a fixed mass of 29.8 Earth masses.

ilar to the isothermal, and another one where the change occurs higher than 1mbar, the shallow temperature is unconstrained and the deep temperature is similar to the isothermal. Essentially, it informs us that the signal mostly arises from pressures around the mbar level, and that an isothermal model of the atmosphere is favored. This is also confirmed by the evidence ratio (see Section 4): the ratio is roughly equal to 1, which means that the two-temperature model is not favoured compared to an isothermal.

We even went a step further and tried a four-temperature model, which posterior distribution is shown in Fig. 5. Again, an isothermal model is entirely compatible with the data, and in that case the evidence ratio is of 3 in favour for the isother-

mal model, showing that isothermal models are very slightly favoured. Given the fact that they require less parameters, we argue that our data are best represented by a constant temperature in the atmosphere.

For a test, we also ran a retrieval with a discrete change in composition at depth but a constant temperature, and a retrieval with two different temperatures in both hemispheres but a constant composition. In all cases, the simple isothermal model/constant composition model is preferred, with a Bayes factor that reaches 20 against the model with two hemispheres.

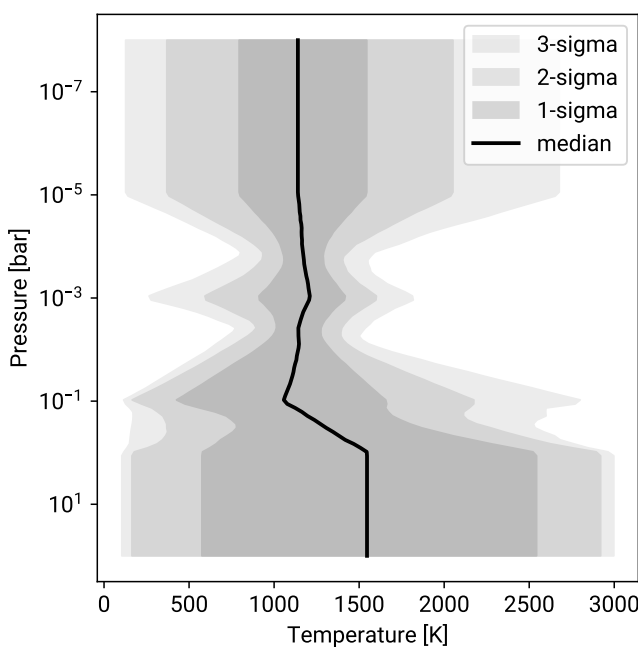


Fig. 5. Posterior distribution for the 4 point temperature-pressure (TP) profile. The solid vertical line indicates the median temperature at a given pressure, the grey shaded lines define the 1σ , 2σ , and 3σ confidence interval (from dark grey to light gray).

3.2.3. Tentative detection of HDO

We searched for rarer molecules, namely isotopologues of water and carbon monoxide. We searched for HDO, H_2^{18}O and ^{13}CO . We could only put upper limits for H_2^{18}O and ^{13}CO , but our retrieval favour the presence of HDO at 2σ . We searched for HDO in correlation maps, and we could not see a significant maximum of correlation from this molecule. We included HDO in our H_2O models but no significant change in the maximum value in the correlation map is observed. However, the Bayes factor (see Sect. 4.2) for a model that includes HDO compared to a model with water and CO only is 12, indicating a strong preference towards a model that contains HDO.

The tentative detection of HDO in the atmosphere of HIP 67522 b yields a $\log_{10}(\text{HDO}/\text{H}_2\text{O}) = -1.4 \pm 0.4$, corresponding to a D/H enrichment factor of ~ 1000 relative to the protosolar value. The implications of this large enrichment are discussed in section 4.3.

In order to assess the robustness of the HDO detection, we ran injection-recovery tests where we injected our best-fit model in the data at $-K_p$ and tried to retrieve the presence of HDO with correlation and nested sampling. Our results are very consistent with the results on the real planet: we do not see anything striking out of the correlation map, but the HDO posterior from the nested sampling peaks at the injected value with a low MMR tail associated with lower likelihood (almost similar to Fig. 4). We also calculated the Bayes factor of a retrieval where we searched for both HDO and H_2O compared to a retrieval with only H_2O , and as in the real data it is around 10. Finally, we injected a model with only water and tried to retrieve both water and HDO. We obtain a flat posterior with a 3σ limit on the MMR at $10^{-4.5}$, and a Bayes factor around one when we include or not HDO in the model. Essentially, our HDO detection is very strong statistically and perfectly consistent with the expectations of injection recovery tests.

4. Discussion

The exceptionally high detection significance of H_2O (20σ) and CO (5σ) in HIP 67522 b far exceeds typical values obtained through ground-based infrared high-resolution transmission spectroscopy of hot Jupiters (e.g., Brogi et al. 2016; Birkby 2018). This remarkable signal strength directly reflects the planet's extreme physical properties: its low mass combined with its inflated radius yields an atmospheric scale height comparable to the planetary radius itself, dramatically enhancing the transmission signal.

The velocity offset of $-2.9 \pm 0.2 \text{ km s}^{-1}$ from the stellar systemic velocity indicates day-to-night atmospheric circulation, as expected for a highly irradiated planet. The upper limit on equatorial rotation ($< 2 \text{ km s}^{-1}$ at 3σ) is consistent with tidal locking and excludes Jupiter-like rotation rates, suggesting that tidal dissipation can already have synchronized this young planet's rotation with its orbital period. This is an important result for constraining star-planet tidal interactions.

Our derived C/O ratio of 0.83 ± 0.09 indicates super-solar composition while our metallicity retrieval favours subsolar values ($[\text{C+O/H}] = -0.8 \pm 0.4$). Both these results are in conflict with the work of Thao et al. (2024), which reported solar C/O ratio but supersolar metallicity. Although their metallicity relies primarily on their 2σ detection of SO_2 —a species we cannot probe effectively in the K-band, this shows that we have a discrepancy as we cannot reconcile JWST and CRIRES+ observational constraints at this stage. Note that our retrieved C/O and metallicity do not depend strongly on whether the mass uncertainty is included as a free parameter in the retrieval or is fixed, and we are therefore confident that they represent correct values for our isothermal models no matter the mass. However, our metallicity is strongly dependent on the presence of clouds: the higher the clouds (up to 0.1 mbar where they would hide the molecular signatures), the larger the metallicity. This degeneracy cannot be resolved by our data alone, but we note that there is no statistical preference for the presence of clouds as the Bayes factor is unity compared to a clear atmosphere (see Sect. 4.2). If we can validate an independent estimate of the metallicity and the mass, we will be able to infer whether the atmosphere is cloudy with a super solar metallicity or cloud free with a lower metal content. We also note that the presence of clouds has an effect on the mass but of only 10% at most (as clouds change the radius by a roughly similar amount), which does not resolve our discrepancy with Thao et al. (2024).

4.1. Mass constraints

The most puzzling result of our paper is the large discrepancy in mass with JWST observations, which disagree at 3σ , favouring a two times more massive planet in our case. Unfortunately, without performing a joint JWST-CRIRES+ retrieval which is out of the scope of this paper, it is unlikely to solve this issue. We can think of two possible flaws that might affect our results: 1) as we fit our radius to the TESS value, we could have an error if there is a strong optical absorber or a very large super-Rayleigh diffusion that would affect the deduced radius because of a much larger atmosphere than predicted in the visible. That would mean that the actual radius used in the gravity estimation is smaller, leading to a smaller mass for a given gravity. This is unlikely, and would need to affect a significant part of the large TESS wavelength range of integration (600–1100 nm roughly) but not impossible. 2) Our results depend on a normalisation factor, which we cannot confirm the validity a posteriori. If there is a normalisation

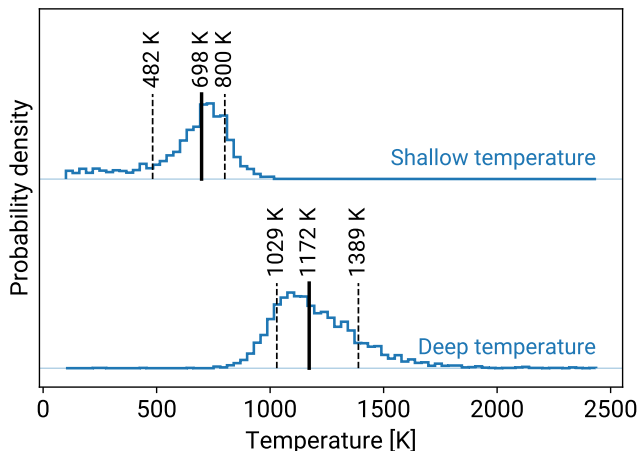


Fig. 6. Posterior distribution for the 2 temperature model using the planet mass derived from the JWST observations where the pressure change occurs deeper than 0.1 mbar.

issue somewhere in our data analysis, that might explain the discrepancy.

If both these caveats are not the source of discrepancy, then the atmospheric model can be the source of error. For example, in Fig. 6, we show the same two-temperature retrieval that we performed in section 3.2.2 but imposing the mass deduced from JWST. In that case, the retrieval excludes an isothermal atmosphere at more than 2σ , whereas it is favoured with our retrieved mass. In this retrieval, the normalisation factor, a , is still not equal to one (indicating an error in the mass) but is larger than in the isothermal model using JWST deduced mass (0.2 in the isothermal case, 0.3 here). Essentially, with a complex temperature and/or composition profile, we might be able to reconcile CRIRES+ and JWST deduced masses (Chabrol et al. in prep.).

4.2. Bayes factor

In this paper, we have compared several different atmospheric models, with different numbers of free parameters. A usual way to perform model comparisons – hence decide whether a model is statistically favoured compared to another – in astrophysics is through the use of Bayesian Information Criterion (BIC) or Akaike Information Criterion (AIC), that are comparisons of the likelihoods of different models penalized by the number of parameters. A model that has a poor likelihood with very few parameters will often be preferred to a model that has a better fit but many more parameters. Such criteria are theoretical approaches to model comparison in the context of studies where the probability are defined relatively to an unknown multiplying factor in the Bayes equation, called the evidence which represents the probability of the data given a model. However, in the context of nested sampling, a measure of the evidence is obtained as an output of the algorithm. We can thus use a more robust criterion for model comparison which is to calculate the evidence ratio (which is a statistical equivalent to Occam’s razor, see the detailed discussion in chapter 28 of Mackay 2003), also called the Bayes factor and often denoted K :

$$K = \frac{P(D|M_1)}{P(D|M_2)} \quad (5)$$

where D are the data, M_1 is a first model and M_2 another one. The rule of thumb criterion to favour M_1 over M_2 is when $K > 3$, with a strong decision towards model 1 if $K > 10$.

With our data, a model that contains water and CO compared to a model that only contains water leads to a Bayes factor of e^{22} , which excludes with certainty the absence of CO in the atmosphere. Regarding complex models, we obtained that the Bayes factor of an isothermal model over a 4 points temperature profile is 3.3 and superior to 20 when comparing to a two hemisphere model, hence favouring the simplest isothermal profile in both cases but without strong preference against the 4 points temperature case. We also discussed in Section 3.2.1 that choosing a mass was favoured upon leaving the mass uncertainty as a free parameter with a Bayes factor of 5, and that the HDO is also strongly favoured when using the evidence ratio.

4.3. HDO/H₂O ratio: signature of strong escape?

The tentative 2σ detection of HDO would represent the first such measurement in an exoplanet atmosphere. It is associated with a Bayes factor of 12, which indicates a strong statistical preference towards the presence of this molecule in the atmosphere. However, if it is real, we must be able to explain the D/H enrichment factor of ~ 1000 relative to the protosolar ratio. This enrichment is unlikely to arise from formation processes (Morley et al. 2019, and private comm. with C. Morley): such extreme deuterium fractionation largely exceeds the primordial ratio measured in protoplanetary disks ($\sim 2 \times 10^{-3}$; Tobin et al. 2023).

The only other known D/H ratio of such extreme value is in Venus’s atmosphere ($\log(\text{HDO}/\text{H}_2\text{O}) \approx -1.5$; Donahue et al. 1982), where ~ 4.5 Gyr of preferential hydrogen escape produced a ~ 100 -fold enrichment relative to Earth. Notably, recent Venus Express analysis revealed that the venusian D/H ratio increases from $\sim 160 \times$ terrestrial at the cloud tops to $\sim 1500 \times$ at 108 km altitude (Mahieux et al. 2024), demonstrating that upper atmospheric layers can be significantly more enriched than the bulk atmosphere. As high-resolution transmission spectroscopy probes the upper atmosphere where photochemical fractionation and escape occur, our measurement may therefore reflect local fractionation in the escaping atmosphere, consistent with predictions that HDO could trace atmospheric evolution in irradiated exoplanets (Morley et al. 2019; Mollière et al. 2019).

For the 17 Myr old HIP 67522 b to achieve comparable enrichment than Venus requires extraordinarily rapid escape rates, plausibly driven by the intense XUV flux from its magnetically active, frequently flaring host star (Ilin et al. 2025b). Enhanced D/H ratios in exoplanet atmospheres due to atmospheric escape are predicted by numerical models (e.g. Cherubim et al. 2024). The D/H ratio provides constraints on the atmospheric escape mechanism, particularly if the He/H ratio is measured as well, which allows to distinguish between competing escape mechanisms. Follow-up observations at higher signal-to-noise and different wavelength ranges are essential to confirm this detection, and to investigate further whether young, highly irradiated planets routinely exhibit signatures of ongoing deuterium fractionation. Observations in the Y-band near the He triplet at 1083 nm will allow to eventually measure He/H if excess Helium absorption is measured in the exoplanet atmosphere. Additionally, as pointed out by Cherubim et al. (2024), deuterium-enhanced planets should be helium-dominated and methane-depleted, meaning that there is a favourable wavelength range to detect HDO at $3.7 \mu\text{m}$, a wavelength range accessible with few high-resolution spectrographs including CRIRES+,

iSHELL (Rayner et al. 2022), and the future Metis instrument at the Extremely Large Telescope (Brandl et al. 2021).

Data availability

The reduced data are available on Zenodo³ (Lavail et al. 2025). The raw data as well as the ESO-processed data are all publicly available one year after the observations at the ESO archive. The planet isothermal synthetic spectra (as well as associated information about opacity sources) are also available at the Zenodo record containing the reduced data.

Acknowledgements. Based on observations made with ESO Telescopes at the La Silla Paranal Observatory under programme ID 114.28HP. We are grateful to the ESO Director General and Director of Science for granting us DDT for this project, to the ESO observing staff, and to Michael Way and Caroline Morley for helpful discussions. F. Debras acknowledges funding from the French National Research Agency (ANR) project ExoATMO (ANR-25-CE49-6598). F. Debras would like to warmly thank the *Action Thématische Physique Stellaire* (ATPS) and *Action Thématische ExoSystèmes* (AT-EXOS) of CNRS/INSU co-funded by CEA and CNES for their financial support. B. Klein., S. Aigrain acknowledge funding from the European Research Council under the European Union's Horizon 2020 research and innovation programme (grant agreement No 865624, GPRV). A. Masson acknowledges support and funds from the grants n° CNS2023-144309 by the Spain Ministry of Science, Innovation and Universities MICIU/AEI/10.13039/501100011033. T. Hood acknowledges funding from the French National Research Agency (ANR) project EXOWINDS (ANR-23-CE31-0001-01). This work was granted access to the HPC resources of CALMIP supercomputing center under the allocation 2021-p21021. This work made use of Astropy: a community-developed core Python package and an ecosystem of tools and resources for astronomy (Astropy Collaboration et al. 2013, 2018, 2022), numpy (Harris et al. 2020). This research has made use of the Astrophysics Data System, funded by NASA under Cooperative Agreement 80NSSC21M0056. This research has made use of the SIMBAD database, operated at CDS, Strasbourg, France. The data reduction process was sped up thanks to GNU parallel (Tange 2023).

Ilin, E., Vedantham, H. K., Poppenhäger, K., et al. 2025b, Nature, 643, 645
 Kanodia, S. & Wright, J. 2018, Research Notes of the American Astronomical Society, 2, 4
 Klein, B., Debras, F., Donati, J.-F., et al. 2024, MNRAS, 527, 544
 Laval, A., Debras, F., & Klein, B. 2025, VLT/CRIRES+ K-band spectroscopy observations of HIP 67522b
 Mackay, D. J. C. 2003, *Information Theory, Inference and Learning Algorithms* (Cambridge University Press)
 Mahieux, A., Viscardi, S., Yelle, R. V., et al. 2024, Proceedings of the National Academy of Science, 121, e2401638121
 Mann, A. W., Newton, E. R., Rizzuto, A. C., et al. 2016, AJ, 152, 61
 Mann, A. W., Wood, M. L., Schmidt, S. P., et al. 2022, AJ, 163, 156
 Mollière, P., Wardenier, J. P., van Boekel, R., et al. 2019, A&A, 627, A67
 Morley, C. V., Skemer, A. J., Miles, B. E., et al. 2019, ApJ, 882, L29
 Nortmann, L., Lesjak, F., Yan, F., et al. 2025, A&A, 693, A213
 Owen, J. E. 2019, Annual Review of Earth and Planetary Sciences, 47, 67
 Plavchan, P., Barclay, T., Gagné, J., et al. 2020, Nature, 582, 497
 Rackham, B. V., Apai, D., & Giampapa, M. S. 2018, ApJ, 853, 122
 Rayner, J., Tokunaga, A., Jaffe, D., et al. 2022, PASP, 134, 015002
 Rizzuto, A. C., Newton, E. R., Mann, A. W., et al. 2020, AJ, 160, 33
 Snellen, I. A. G., de Kok, R. J., de Mooij, E. J. W., & Albrecht, S. 2010, Nature, 465, 1049
 Tange, O. 2023, GNU Parallel 20231122 ('Grindavík')
 Thao, P. C., Mann, A. W., Feinstein, A. D., et al. 2024, AJ, 168, 297
 Tobin, J. J., van't Hoff, M. L. R., Leemker, M., et al. 2023, Nature, 615, 227

References

Astropy Collaboration, Price-Whelan, A. M., Lim, P. L., et al. 2022, ApJ, 935, 167
 Astropy Collaboration, Price-Whelan, A. M., Sipőcz, B. M., et al. 2018, AJ, 156, 123
 Astropy Collaboration, Robitaille, T. P., Tollerud, E. J., et al. 2013, A&A, 558, A33
 Barber, M. G., Thao, P. C., Mann, A. W., et al. 2024, ApJ, 973, L30
 Baruteau, C., Bai, X., Mordasini, C., & Mollière, P. 2016, Space Sci. Rev., 205, 77
 Birkby, J. L. 2018, in *Handbook of Exoplanets*, ed. H. J. Deeg & J. A. Belmonte, 16
 Blain, D., Mollière, P., & Nasedkin, E. 2024, The Journal of Open Source Software, 9, 7028
 Brandl, B., Bettinovil, F., van Boekel, R., et al. 2021, The Messenger, 182, 22
 Brogi, M., de Kok, R. J., Albrecht, S., et al. 2016, ApJ, 817, 106
 Brogi, M., & Line, M. R. 2019, AJ, 157, 114
 Buchner, J., Georgakakis, A., Nandra, K., et al. 2014, A&A, 564, A125
 Cherubim, C., Wordsworth, R., Hu, R., & Shkolnik, E. 2024, ApJ, 967, 139
 David, T. J., Petigura, E. A., Luger, R., et al. 2019, ApJ, 885, L12
 Debras, F., Klein, B., Donati, J.-F., et al. 2024, MNRAS, 527, 566
 Donahue, T. M., Hoffman, J. H., Hodges, R. R., & Watson, A. J. 1982, Science, 216, 630
 Dorn, R. J., Bristow, P., Smoker, J. V., et al. 2023, A&A, 671, A24
 Feroz, F. & Hobson, M. P. 2008, MNRAS, 384, 449
 Feroz, F., Hobson, M. P., & Bridges, M. 2009, MNRAS, 398, 1601
 Gibson, N. P., Merritt, S., Nugroho, S. K., et al. 2020, MNRAS, 493, 2215
 Gibson, N. P., Nugroho, S. K., Lothringer, J., Maguire, C., & Sing, D. K. 2022, MNRAS, 512, 4618
 Harris, C. R., Millman, K. J., van der Walt, S. J., et al. 2020, Nature, 585, 357
 Heitzmann, A., Zhou, G., Quinn, S. N., et al. 2021, ApJ, 922, L1
 Hood, T., Debras, F., Moutou, C., et al. 2024, A&A, 687, A119
 Ilin, E., Bloot, S., Callingham, J. R., & Vedantham, H. K. 2025a, A&A, 699, A147

³ <https://doi.org/10.5281/zenodo.17909093>

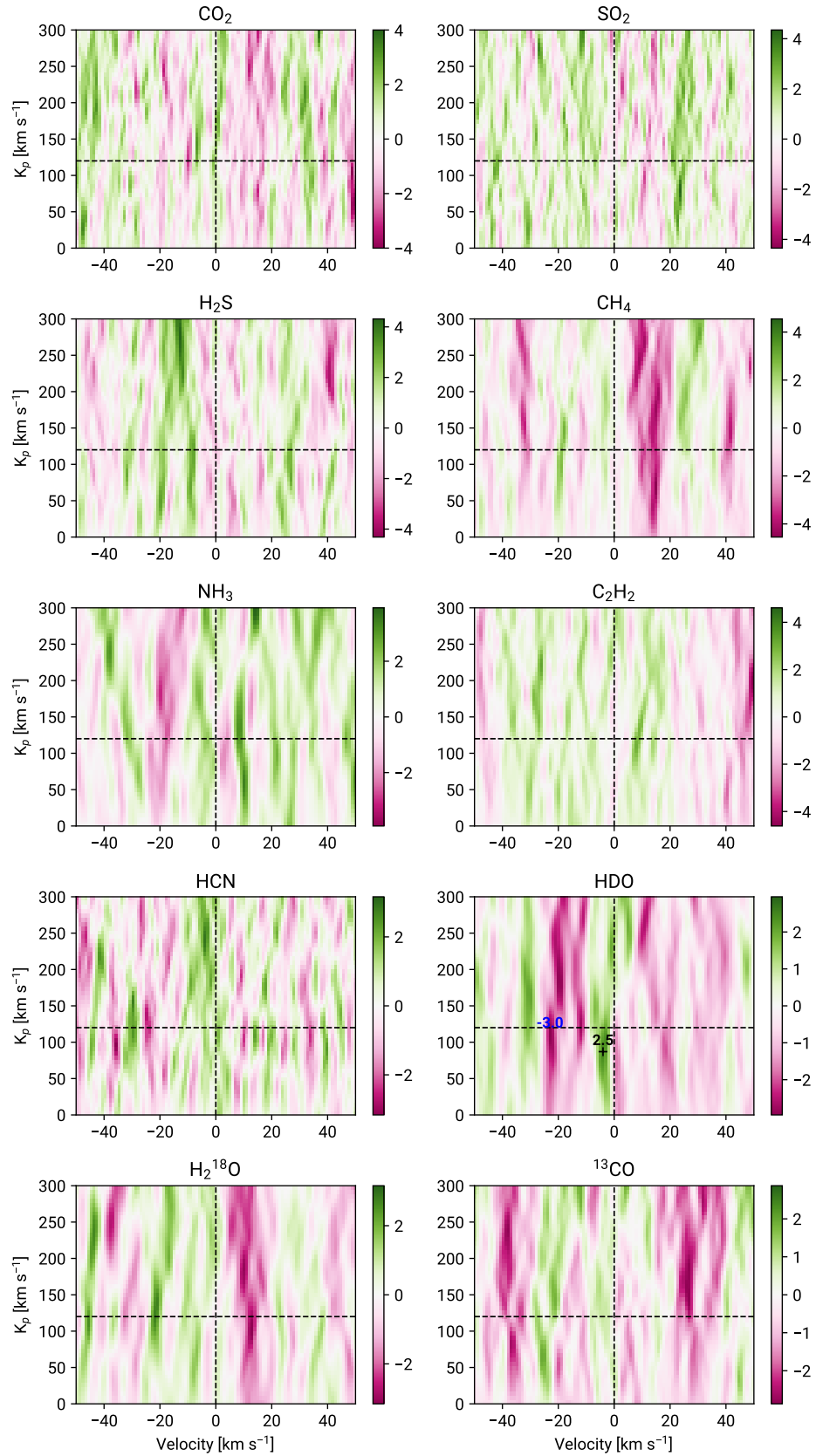


Fig. 7. Same as Fig. 3 for all the non-detected species.